Bismuth oxybromide/reduced graphene oxide heterostructure sensitized with Zn-tetracarboxyphthalocyanine as a highly efficient photocatalyst for the degradation of Orange II and phenol

Seydou Ouedraogo, Bilel Chouchene, Thomas Gries, Christophe Desmarets, Lavinia Balan, Jean-Jacques Gaumet, Ghouti Medjahdi, Karifa Bayo, Raphaël Schneider

Bismuth oxybromide/reduced graphene oxide heterostructure sensitized with Zn-tetracarboxyphthalocyanine as a highly efficient photocatalyst for the degradation of Orange II and phenol

Seydou Ouedraogo[a], Bilel Chouchene[b], Thomas Gries[c], Christophe Desmarets[d], Lavinia Balan[e], Jean-Jacques Gaumet[f], Ghouti Medjahdi[c], Karifa Bayo[a], Raphaël Schneider[*b]

[a] Laboratoire de chimie moléculaire et des matériaux, Université Joseph Ki-Zerbo, 03 BP 7021 Ouagadougou, Burkina Faso

[b] Université de Lorraine, CNRS, LRGP, F-54000 Nancy, France

[c] Université de Lorraine, CNRS, IJL, F-54000 Nancy, France

[d] Institut Parisien de Chimie Moléculaire UMR-CNRS 8232, Sorbonne Université 4 Place Jussieu, 75252 Paris cedex 5, France

[e] CEMHTI-UPR 3079 CNRS, Site Haute Température, 1D avenue de la Recherche Scientifique, 45071 Orléans, France

[f] Université de Lorraine, LCP-A2MC, Institut Jean Barriol, 1 bd Arago, F-57070 Metz, France

E-mail: raphael.schneider@univ-lorraine.fr

Abstract

The preparation of heterostructured photocatalysts associating BiOBr, reduced graphene oxide (rGO) and zinc tetracarboxyphthalocyanine ($ZnPc(CO_2H)_4$) and their performance for the degradation of the Orange II dye and of phenol are reported. The BiOBr/rGO/$ZnPc(CO_2H)_4$(0.25) photocatalyst displays a superior activity than BiOBr and BiOBr/rGO, indicating that $ZnPc(CO_2H)_4$ enhances both the visible light absorption and the charge carrier separation, which is confirmed by photoluminescence, photocurrent responses and electrochemical impedance spectroscopy Nyquist plots. Scavenging experiments show that the main active species involved in the degradation of Orange II and phenol are superoxide radicals and holes and a mechanism is proposed. Due to its high stability, the BiOBr/rGO/$ZnPc(CO_2H)_4$(0.25) catalyst shows high potential for real environmental remediation.

Keywords: Bismuth oxybromide, reduced graphene oxide, zinc tetracarboxyphthalocyanine, heterostructured photocatalyst, photodegradation

1. Introduction

Bismuth oxyhalides BiOX (X = Cl, Br or I) are emerging semiconductors that exhibit a high potential for photocatalytic environmental decontamination and energy conversion due to their low cost, high chemical and photostability and unique crystalline structure [1-4]. Bismuth oxyhalides exhibit a tetragonal structure composed of $[Bi_2O_2]^{2+}$ layers stacked along the *c*-axis by two layers of X^- ions via van der Walls forces. The [X-Bi-O-Bi-X] structure provides an internal electric field along the [001] direction of BiOX that promotes the effective separation of photogenerated electron-hole pairs and thus the photocatalytic activity [1-4].

BiOBr has been proved to be an efficient photocatalyst for the degradation of organic pollutants [5-10]. However, BiOBr suffers from various drawbacks including its wide energy bandgap (ca. 2.8 eV) that limits its utilization of visible light below 440 nm and from the high recombination rate of photogenerated electron-hole pairs. In recent years, various strategies have been developed to overcome these problems. The construction of heterostructured photocatalysts in which BiOBr is coupled with graphene derivatives [11-13], with small bandgap semiconductors like WS_2 [14], BiOI [15], CdS [16,17], $CuInS_2$ [18] or $ZnFe_2O_4$ [19] or with metal nanoparticles like Bi or Pt [20,21] has been demonstrated to be efficient for improving both the charge separation and transportation and increasing the visible light absorption.

Metal porphyrins and phthalocyanines (Pcs) have gained high interest in the field of photocatalysis due to their photosensitizing properties in the visible and NIR range and to their high photostability. Numerous studies have demonstrated that Pcs can activate wide bandgap semiconductors like TiO_2 [22,23], ZnO [24,25] or graphitic carbon nitride C_3N_4 [26,27]. The coupling of BiOX with porphyrins and Pcs has been the subject of far fewer studies. Sn-porphyrins were successfully coupled with BiOCl or BiOCl/BiOBr to engineer photocatalysts for the degradation of dyes [28,29]. Heterostructured photocatalysts associating CuPc and BiOCl were developed for the degradation of Rhodamine B and for water splitting [30,31].

More recently, a FePc was coupled with BiOBr to engineer photocatalysts with enhanced visible light response that were used for the degradation of tetracyclin and ciprofloxacin [32]. Another key advantage of Pcs is their synthetic flexibility that allows to easily modify the peripheral substituents. A few studies demonstrated that carboxylic acid-functionalized Pcs strongly bound to the surface of semiconductors and thus allow their effective photosensitization and the transfer of an electron from their excited state to the conduction band of the semiconductor [26, 33,34].

Herein, zinc tetracarboxyphthalocyanine ($ZnPc(CO_2H)_4$) was first the time demonstrated to be an effective photosensitizer for a composite photocatalyst associating BiOBr and reduced graphene oxide (rGO). The BiOBr/rGO/$ZnPc(CO_2H)_4$ heterostructured catalysts were easily prepared by sonicating $ZnPc(CO_2H)_4$ and BiOBr/rGO. A loading of 0.25 wt% in $ZnPc(CO_2H)_4$ was found to be optimal to obtain a photocatalyst with an enhanced activity compared to BiOBr/rGO for the degradation of the Orange II dye and of phenol under visible and simulated solar light, respectively. The association of BiOBr/rGO with $ZnPc(CO_2H)_4$ was demonstrated to improve both the harvesting of visible light and the lifetime of photogenerated charge carriers. The photodegradation mechanism was investigated in detail and the active species involved were identified as superoxide radicals $O_2^{\bullet-}$ and holes. Finally, the BiOBr/rGO/$ZnPc(CO_2H)_4$(0.25) photocatalyst exhibits a high stability during repeated photodegradation of phenol, which shows its high potential for real photocatalytic applications.

2. Experimental section

2.1. Materials

$Bi(NO_3)_3 \bullet 5H_2O$ (>99.99%, Sigma), KBr (>99%, Sigma), NaOH (> 97%, Sigma) and ethanol were used as received without further purification. Reduced graphene oxide was prepared as previously described [35]. All solutions were prepared using Milli-Q water (18.2 MΩ.cm, Millipore) as solvent.

2.2. Synthesis of the BiOBr/rGO composite

The BiOBr/rGO composite was prepared by a hydrothermal reaction [13]. Briefly, $Bi(NO_3)_3 \bullet 5H_2O$ (4 mmol) and rGO (1 wt% relative to BiOBr) were dispersed under sonication in 36 mL of 1M HNO_3. Separately, KBr (4 mmol) was dissolved into 12 mL of HNO_3 (1M). After KBr was dissolved completely, it was added dropwise to the $Bi(NO_3)_3$-rGO mixture and the solution further stirred at room temperature for 30 min. Next, the mixture was transferred into a 100 mL Teflon-lined stainless autoclave which was held at 160 °C for 12 h. After natural cooling, the BiOBr/rGO solid was recovered by centrifugation (4000 rpm for 15 min), washed with absolute ethanol (4 x 20 mL) and then dried at 70 °C for 12 h.
BiOBr was prepared using the same synthetic protocol.

2.3. Synthesis of $ZnPc(CO_2H)_4$

$ZnPc(CO_2H)_4$ was synthesized from trimellitic anhydride, urea, zinc acetate and hexaammonium heptamolybdate in refluxing nitrobenzene [36]. Briefly, trimellitic anhydride (8.16 g, 42.47 mmol), $Zn(OAc)_2 \bullet 2H_2O$ (2.33 g, 10.62 mmol), urea (10 g, 166.50 mmol) and $(NH_4)_6Mo_7O_{24} \bullet 4H_2O$ (1 mg, 8.59 10^{-4} mmol) were solubilized into 30 mL of nitrobenzene and the mixture was refluxed for 8 h. The solution turns green after 15 min of heating then a green precipitate is formed. After cooling to room temperature, the reaction mixture is filtered and the green solid obtained is first washed with hot water and then with ethanol before being crushed. The solid is further washed in a Soxhlet apparatus with toluene, ethanol, methanol and acetone for 48 h. The solid is then treated with a hot 10% HCl solution for 15 min and then washed with water until neutral and finally with acetone before being dried at 120°C for 24 h in vacuum. $ZnPc(CO_2H)_4$ was obtained with a 65% yield.

2.4. Synthesis of BiOBr/rGO/$ZnPc(CO_2H)_4$ photocatalysts

BiOBr/rGO/$ZnPc(CO_2H)_4$ catalysts were prepared by sonication of BiOBr/rGO (500 mg) and $ZnPc(CO_2H)_4$ (0.25 and 0.5 wt% relative to BiOBr/rGO) in 5 mL of DMF for 30 min. After centrifugation (4000 rpm for 15 min), the solid obtained was dried in an oven at 70°C for 12 h before being heated at 150°C for 2 h in order to anchor the Pc at the surface of the BiOBr/rGO heterostructure and to eliminate any trace of solvent.

2.5. Photocatalytic tests

Photocatalytic experiments were performed through the degradation of Orange II and phenol, both used at a concentration of 10 mg/L. The light source was an Osram Ultra Vitalux lamp equipped with an UV cutoff filter (> 420 nm) for Orange II and without UV filter for phenol. The light intensity at the surface of the dye solution was estimated to be 13 mW/cm^2 for Orange II and 15 mW/cm^2 for phenol. In a typical reaction, 30 mg of the catalyst was dispersed in 30 mL of pollutant and the mixture stirred 30 min in the dark to achieve the adsorption/desorption equilibrium. Next, light was turned on. At given intervals of illumination, samples (2 mL) of the reaction solution were taken out, centrifuged (15,000 rpm for 2 min) to remove the photocatalyst and analyzed. The concentration of Orange II and phenol was determined by measuring the absorbance at 485 and 268 nm, respectively, using a UV-visible spectrophotometer. The concentration of phenol was also monitored by liquid chromatography/mass spectrometry (LC/MS).

To investigate the active species generated during the photodegradation process, experiments were conducted using *tert*-butanol (*t*-BuOH, 10 mM), 4-hydroxy-2,2,6,6-tetramethylpiperidine-1-oxyl (TEMPOL, 10 mM), DMSO (10 mM), ammonium oxalate (OA, 10 mM) and sodium azide (NaN_3, 10 mM) as scavengers of $^{\bullet}OH$ and $O_2^{\bullet-}$ free radicals, electrons and holes, and singlet oxygen $^1O_2$, respectively.

2.6. Instrumentation

X-ray diffraction (XRD) analyzes were conducted using a Panalytical X'Pert pro MPD diffractometer using Cu Kα radiation (wavelength = 0.15405 nm). Scanning electron microscopy (SEM, JEOL JSM-6490 LV and JEOL JSM IT800) was applied to investigate the crystals morphology and shape. Transmission electron microscopy (TEM) images were taken using a Philips (CM200, 200 kV) microscope. The surface states and chemical composition of the catalysts were determined by X-ray photoelectron spectroscopy (XPS) using Gammadata Scienta SES 200-2 spectrometer. The surface area and porosity of the composites were examined by N_2 absorption/desorption at 77 K using a Micromeritics TRISTAR II Plus instrument. The samples are first degassed for 12 h under vacuum at 150 °C. The resulting isotherms were analyzed using the BET method (Brunauer-Emmett-Teller) while the porosity

was determined using the (Barrett-Joyner-Halenda) (BJH) method. The zeta potential of the samples was determined using Malvern Zetasizer Nano ZS equipment. Inductively Coupled Plasma-Optical Emission Spectrometer (ICP-OES) measurements were conducted on a Varian 720-ES equipment.

All the optical properties were recorded under ambient conditions. Fourier transform infrared spectra were recorded using a Brucker ALPHA spectrometer. The UV-visible spectra for liquid samples were recorded on a Thermo Scientific Evolution 220 UV-Visible spectrometer. The UV-visible spectra of solid samples were measured using a Shimadzu 2600-2700 UV-visible spectrometer in diffuse reflectance mode. The photoluminescence (PL) spectra were recorded with a Horiba Fluoromax-4 Jobin Yvon spectrofluorimeter. The Raman spectra were recorded on a Horiba Scientific Xplora spectrometer with 532 nm wavelength incident laser light.

The electrochemical properties were measured in a quartz beaker; the signals were recorded using SP150 Biologic potentiostat in a standard three electrode system. Ag/AgCl saturated with KCl acted as reference electrode, a Pt coiled wire used as counter electrode and FTO glass coated with BiOBr or BiOBr/rGO or BiOBr/rGO/ZnPc$(CO_2H)_4$ with a surface area of 1 cm^2 as the working electrode. An aqueous solution of Na_2SO_4 (0.1 M) was prepared as the electrolyte. The applied voltage was E = + 0.5 V vs. the reference electrode.

A Velos Pro (Thermo Fisher Scientific) linear ion trap mass spectrometer was used with Flow Injection Analysis (FIA-MS) monitoring of phenol degradation via atmospheric pressure chemical ionization (APCI). Single ion monitoring (SIM) was used for the detection on the negative ion mode for measuring the $[M-H]^-$ signal at m/z 93 (M = Ph). The analysis was repeated three times in a row with a 20 μL injection.

The cyclic voltammetry (CV) was carried out with an Autolab PGSTAT 100 workstation (Metrohm) controlled by an external PC and using a standard three-electrode setup at 25°C. Working vitreous carbon electrode (3 mm diameter) was polished with 6 μm diamond paste. A Pt wired served as counter electrode while a calomel electrode (SCE) LiCl 1M was employed as reference electrode and separated from the bulk by a double bridge. Electrochemical grade *tetra*-butylammonium hexafluorophosphate employed as the supporting electrolyte in commercially anhydrous DMF at a concentration of 10^{-1} mol/L. Typically, the solution of ZnPc$(CO_2H)_4$ was purged with argon flow 10 min, and the voltammogram was recorded at ambient temperature with a scan rate of 20 mV/s. The CV was done using ferrocene/ferrocenium (Fc/Fc^+) redox couple as an external standard. The energy level of

Fc/Fc+ was assumed at -4,8 eV to vacuum [37]. The corresponding HOMO level was calculated using E_{ox} (onset) for the measurements in the solution. The estimations were done with the empirical relation E_{HOMO} = - [(E_{ox}-$E_{1/2\ (ferrocene)}$ + 4,8] eV, where E_{ox} and $E_{1/2\ (ferrocene)}$ are respectively the onset oxidation potential electrode and half-wave potential of ferrocene relative to the reference electrode [38,39]. The LUMO energy level was calculated by adding the optical band gap value from the respective HOMO energy level $E_{LUMO} = E_{HOMO} + E_{g,opt}$.

3. Results and discussion

3.1. Photocatalysts synthesis and characterization

BiOBr/rGO/ZnPc$(CO_2H)_4$ photocatalysts were prepared by sonicating the BiOBr/rGO composite with ZnPc$(CO_2H)_4$ in DMF followed by drying and a mild heat treatment at 150°C for 2 h (Scheme 1). Loadings of 0.1, 0.25 and 0.5 wt% in ZnPc$(CO_2H)_4$ relative to BiOBr/rGO were used.

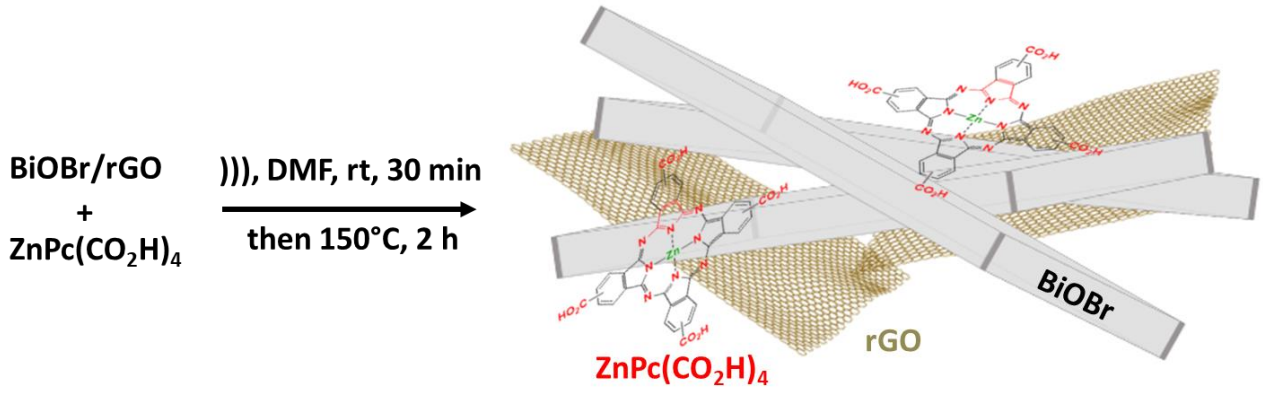

Scheme 1. Synthetic route used for the preparation of the BiOBr/rGO/ZnPc$(CO_2H)_4$ heterostructured photocatalysts.

The phase purity of the samples was first determined by XRD (Fig. 1a). All reflections can be indexed to the tetragonal phase of BiOBr (JCPDS file No 00-009-0393) (Fig. S1). Due to the small amount of rGO (1 wt%) and ZnPc$(CO_2H)_4$ (0.1, 0.25 or 0.5 wt%) associated to BiOBr, these compounds were not detected by XRD. No impurities were observed which suggests the successful preparation of the BiOBr/rGO/ZnPc$(CO_2H)_4$ heterostructures.

The structure of the catalysts was further investigated by Raman spectroscopy (Fig. 1b). As BiOBr belongs to the P4/nmm space group, the signal at 109 cm^{-1} can be assigned to the A_{1g} internal stretch mode [40]. The weaker band observed at 150 cm^{-1} corresponds to the E_{1g} Bi-Br stretching mode. No deterioration or decrease of the signals was observed after association with rGO and $ZnPc(CO_2H)_4$ indicating that the crystalline structure of BiOBr was well maintained. The D and G bands of rGO located at 1341 and 1577 cm^{-1}, respectively, are of low intensity and overlap signals at 1339 and 1566 cm^{-1} that are the characteristic signature of metal cation-phthalocyanine complexes [41,42]. A shift of these signals to 1345 and 1604 cm^{-1}, respectively, confirms the binding of $ZnPc(CO_2H)_4$ with BiOBr/rGO.

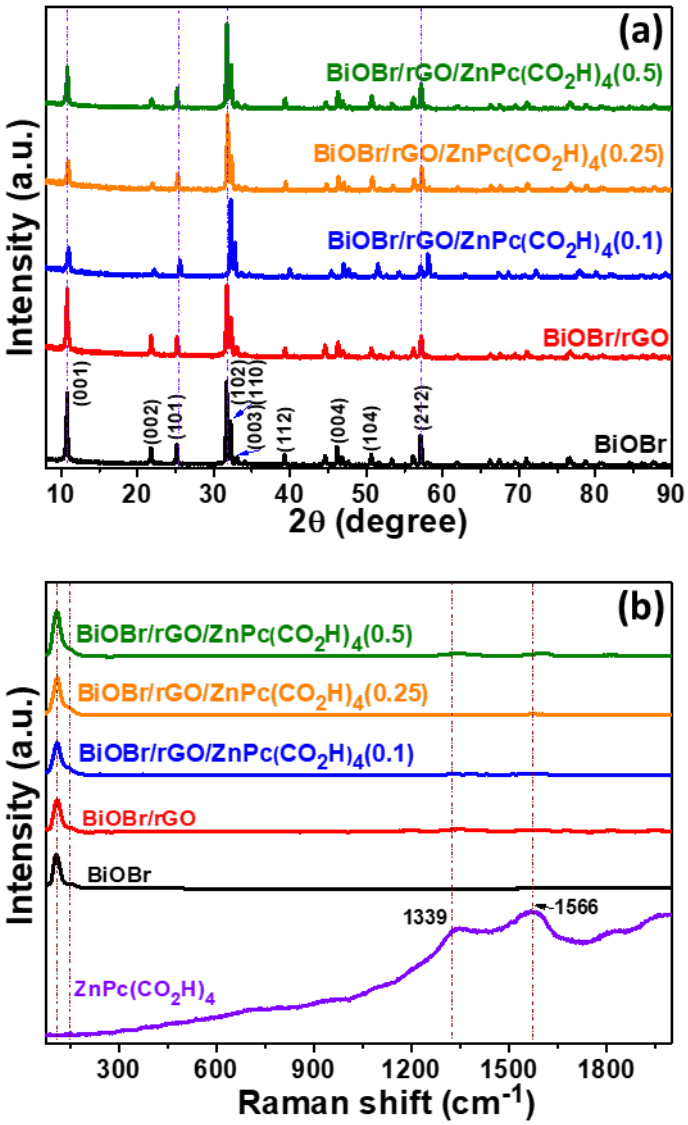

Fig. 1. (a) XRD patterns of BiOBr, BiOBr/rGO and of BiOBr/rGO/$ZnPc(CO_2H)_4$ catalysts, (b) Raman spectra of $ZnPc(CO_2H)_4$, BiOBr, BiOBr/rGO and BiOBr/rGO/$ZnPc(CO_2H)_4$ catalysts.

FT-IR spectroscopy was further used to evidence the structure of the BiOBr/rGO/ZnPc$(CO_2H)_4$ hybrid samples (Fig. 2). For ZnPc$(CO_2H)_4$, the broad signal centered at 3182 cm^{-1} corresponds to the stretching of the hydroxyl groups of the carboxylic acid functions and the carbonyl ($\gamma_{C=O}$) vibration appears at 1717 cm^{-1}. Pure BiOBr shows a sharp signal at 501 cm^{-1} which can be assigned to the Bi-O stretching vibration mode in the tetragonal crystal phase [43]. After association of BiOBr with rGO, the characteristic vibrational signals of rGO at 2992 and 2899 cm^{-1} (γ_{C-H}), 1721 cm^{-1} ($\gamma_{C=O}$), 1654-1225 cm^{-1} (γ_{C-C}) and 1071 cm^{-1} (γ_{C-O}) can be observed. The spectral signature of ZnPc$(CO_2H)_4$ is close to that of rGO and could not clearly be observed for the BiOBr/rGO/ZnPc$(CO_2H)_4$ catalysts.

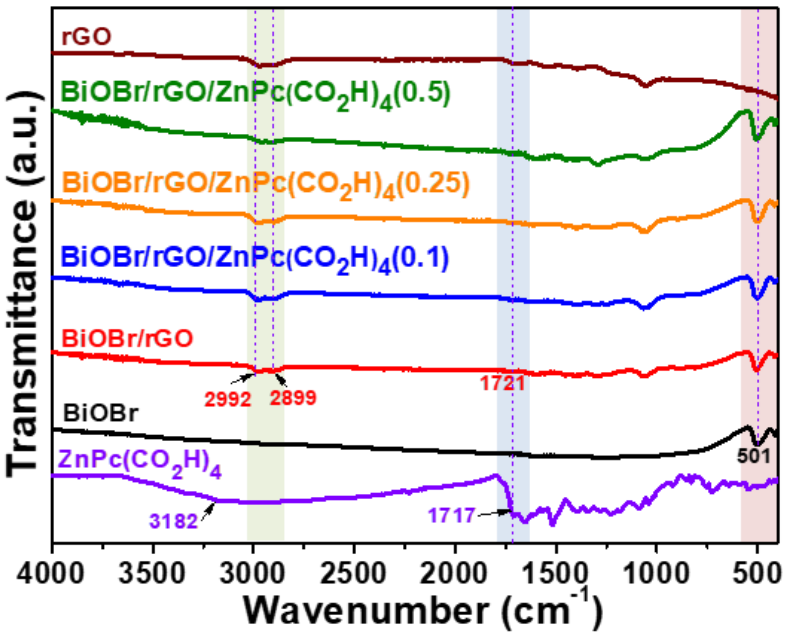

Fig. 2. FT-IR spectra of ZnPc$(CO_2H)_4$, BiOBr, rGO, BiOBr/rGO and of BiOBr/rGO/ZnPc$(CO_2H)_4$ composites.

As the light absorption capacity of the photocatalysts plays a key role on their activity, UV-visible absorption spectra of ZnPc$(CO_2H)_4$ and of BiOBr, BiOBr/rGO and BiOBr/rGO/ZnPc$(CO_2H)_4$ catalysts were analyzed (Fig. S2 and Fig. 3). The UV-visible absorption spectrum of ZnPc$(CO_2H)_4$ shows the B-bands at 270 and 346 nm and the Q-bands at 613, 678 and 686 nm (Fig. S2a). The splitting observed for the signals at 678 and 686 likely originates from the presence of isomers of ZnPc$(CO_2H)_4$. The Q-bands at 678 and 686 nm correspond to

the π-π* transitions from the HOMO to the LUMO of $ZnPc(CO_2H)_4$ while the weak signal at 613 nm indicates the presence of a dimer formed via π-stacking and/or hydrogen bonding between carboxylic acid groups [44]. These signals clearly demonstrate the non-aggregated state of the Pc. After excitation at 400 nm, a broad PL emission centered at ca. 500 nm and a much well resolved one at 691 nm were observed (Fig. S2b).

The absorption edge of pure BiOBr is of ca. 435 nm, indicating a weak absorption in the visible region (Fig. 3a). After association with rGO, the visible absorption increases indicating that strong chemical bonds were created between BiOBr and rGO. For BiOBr/rGO/$ZnPc(CO_2H)_4$ hybrids, the absorption signals of the phthalocyanine can be observed at 637 and 701 nm and are red-shifted compared to the pure $ZnPc(CO_2H)_4$, further confirming the strong interaction between BiOBr/rGO and $ZnPc(CO_2H)_4$. The enhanced visible light absorption of BiOBr/rGO/$ZnPc(CO_2H)_4$ composites should promote the generation of electron-hole pairs, and thus improve the photocatalytic performance. The bandgap energy (*E*g) of BiOBr, BiOBr/rGO and BiOBr/rGO/$ZnPc(CO_2H)_4$(0.1, 0.25 and 0.5) were determined using the formula $(\alpha h\gamma)^n = A(h\gamma - Eg)$ where α is the absorption coefficient, h is the Plank constant, γ is the optical frequency and n = ½ for the indirect bandgap BiOBr semiconductor and were found to be 2.86, 2.87, 2.84, 2.84 and 2.81 eV for BiOBr, BiOBr/rGO, BiOBr/rGO/$ZnPc(CO_2H)_4$(0.1), BiOBr/rGO/$ZnPc(CO_2H)_4$(0.25) and BiOBr/rGO/$ZnPc(CO_2H)_4$(0.5), respectively (Fig. 3b).

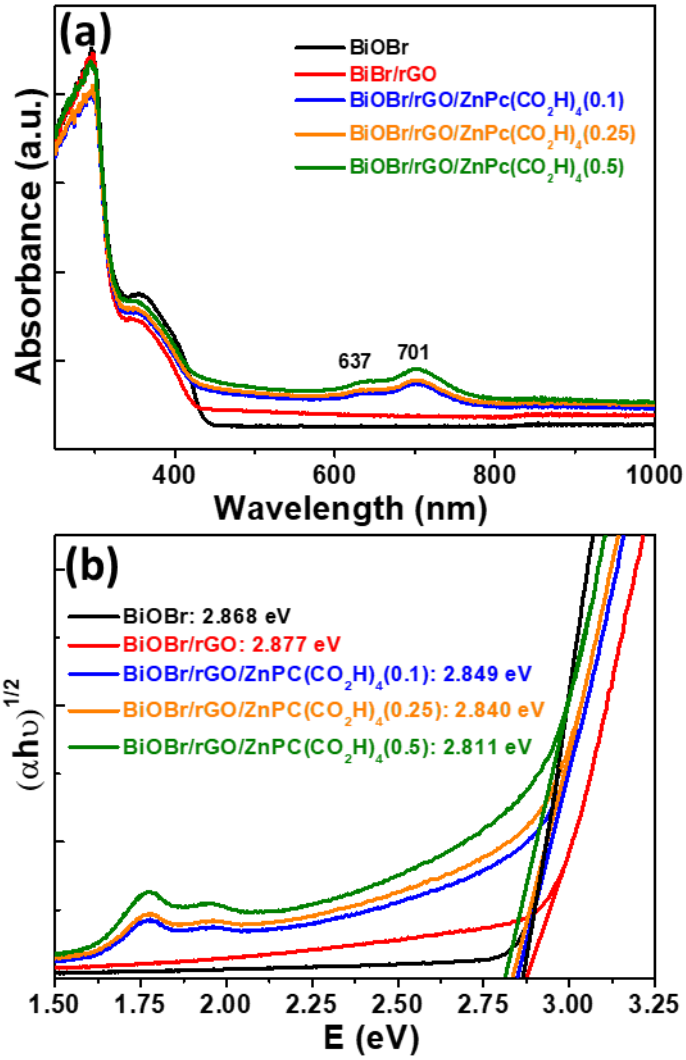

Fig. 3. UV-visible diffuse reflectance spectra (DRS) of BiOBr, BiOBr/rGO and BiOBr/rGO/ZnPc$(CO_2H)_4$ catalysts and (b) the corresponding bandgap energies.

The morphologies of the catalysts were first revealed by SEM (Fig. 4). Stacked quadrilateral-like microplates with an average length of ca. 4 µm and a thickness of 200 nm can be observed for BiOBr and BiOBr/rGO (Fig. 4a,b). No specific organization of the microplates such as microsphere or flower can be observed. The microplate morphology is typical of BiOBr particles prepared in acidic medium [13]. BiOBr plates appear as broken for the BiOBr/rGO/ZnPc$(CO_2H)_4$(0.25) photocatalyst likely due to sonication treatment used to assemble BiOBr/rGO with ZnPc$(CO_2H)_4$ (Fig. 4c). The association of ZnPc$(CO_2H)_4$(0.25) and its relative uniform dispersion at the surface of BiOBr sheets was demonstrated by the energy dispersive X-ray spectroscopy (EDX) mapping (Fig. 4d-i).

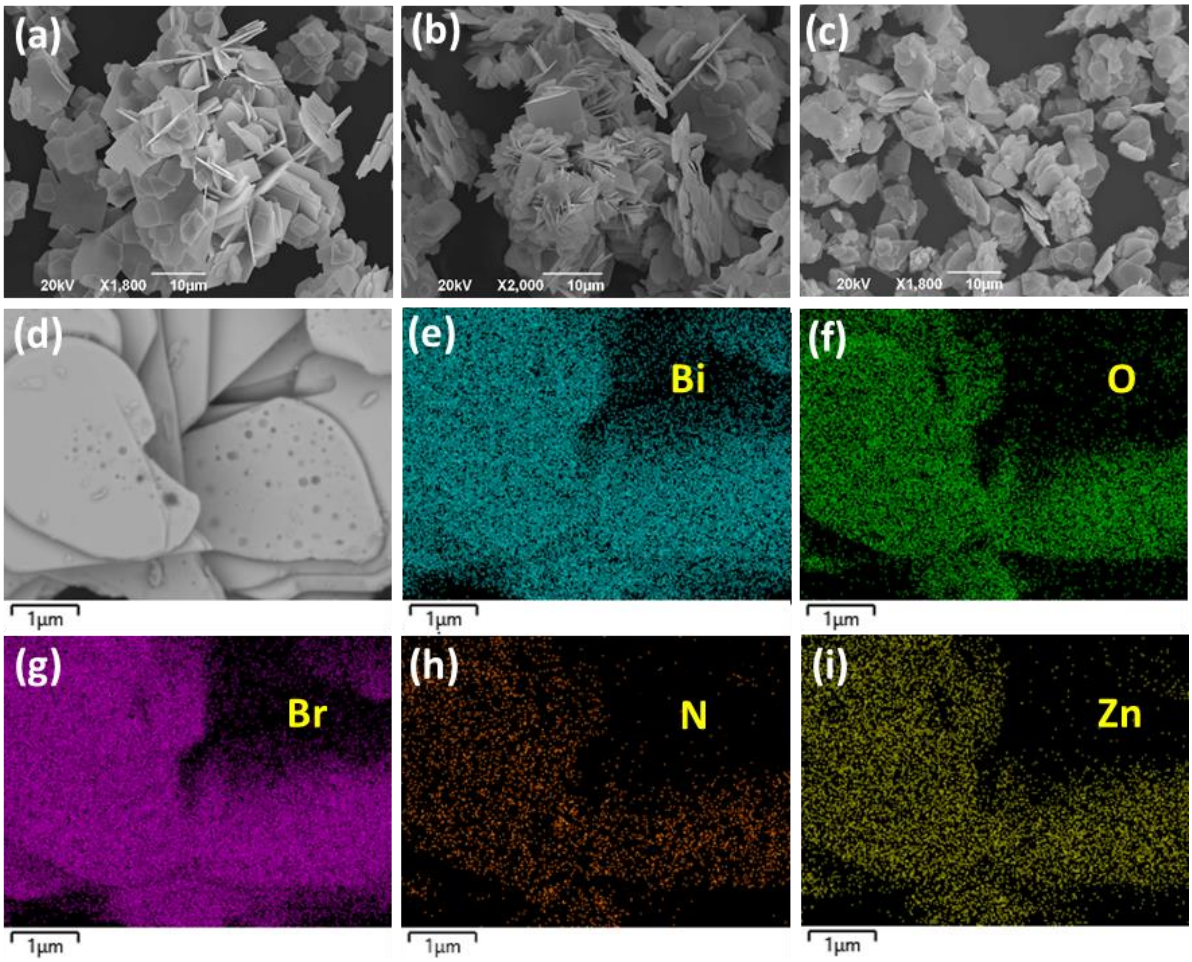

Fig. 4. SEM images of (a) BiOBr, (b) BiOBr/rGO and (c) BiOBr/rGO/ZnPc$(CO_2H)_4$(0.25) catalysts. (d) SEM image of the BiOBr/rGO/ZnPc$(CO_2H)_4$(0.25) catalyst and (e-i) the corresponding elemental mapping of Bi, O, Br, N and Zn elements, respectively.

TEM was further used to characterize the morphology and the microstructure of the BiOBr/rGO and BiOBr/rGO/ZnPc$(CO_2H)_4$(0.25) composites. A typical 2D plate structure with a smooth surface can be observed for the BiOBr/rGO sample (Fig 5a-b). The associated EDX analysis shows that the sample contains the Bi, O, Br and C elements (Fig. 5c). After coupling with ZnPc$(CO_2H)_4$, small clusters can be observed at the surface of BiOBr/rGO microplates, suggesting that ZnPc$(CO_2H)_4$ deposits on their surface (Fig. 5d-e). This was further confirmed by EDX in which the Zn and N elements were detected (Fig. 5f). The close contact between BiOBr/rGO microplates and ZnPc$(CO_2H)_4$ should promote the charge transportation and separation and thus improve the photocatalytic activity.

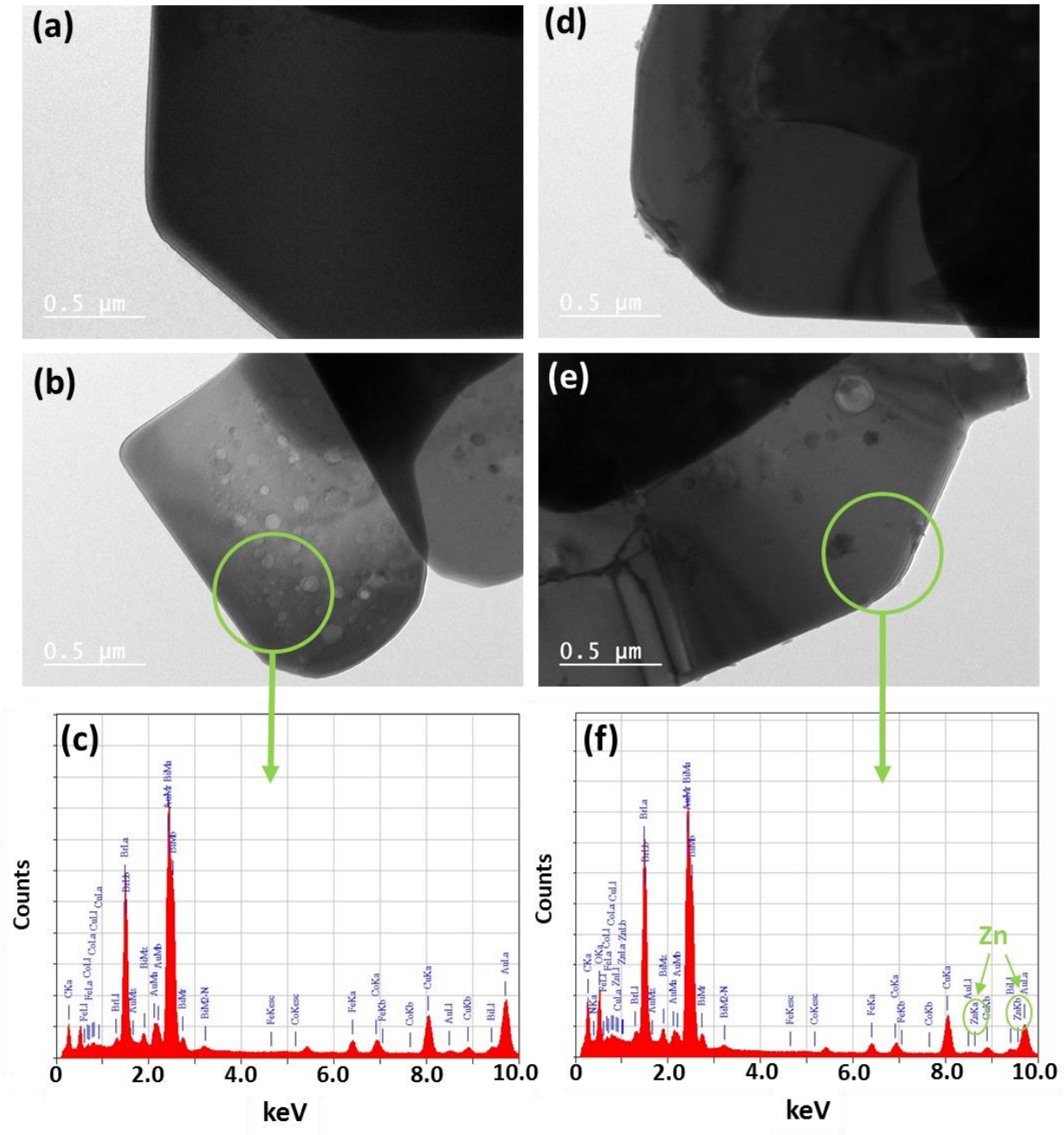

Fig. 5. TEM images of (a,b) BiOBr/rGO and (d,e) BiOBr/rGO/ZnPc$(CO_2H)_4$(0.25). (c) and (f) are the corresponding EDX analyses.

The specific surface areas of BiOBr, BiOBr/rGO and BiOBr/rGO/ZnPc$(CO_2H)_4$(0.25) and the pore size distributions were investigated using nitrogen adsorption-desorption isotherms (Fig. S3, Table S1). The isotherms are of type IV according to the IUPAC classification, indicating the mesoporous structures of the samples (Fig. S3a). The BET surface area of BiOBr is of 7.46 m^2/g. After association with rGO, the BET surface area slightly increases (13.04 m^2/g) and then

slightly decreases after coupling with $ZnPc(CO_2H)_4$ (10.13 m^2/g). An increase of the pore diameter from 6.78 to 8.46 nm was also observed after association of BiOBr with rGO and $ZnPc(CO_2H)_4$, which should favor the diffusive transport of photogenerated charge carriers to the surface of the photocatalyst (Fig. S3b). However, the relatively modest BET surface areas measured for BiOBr, BiOBr/rGO and BiOBr/rGO/$ZnPc(CO_2H)_4$(0.25) suggest that they should not play a key role on the photocatalytic activity.

The chemical states and the elemental composition of the BiOBr/rGO/$ZnPc(CO_2H)_4$(0.25) catalyst selected as representative were further investigated by XPS. Bi, O, Br, C, N and Zn can be observed on the XPS survey spectrum (Fig. S4), indicating the high purity of the photocatalyst. The Bi $4f_{5/2}$ and Bi $4f_{7/2}$ signals appear at 164.66 and 159.31 eV and confirm that Bi exhibits the +3 oxidation state [45] (Fig. 6a). For O 1s, the peaks at 530.20, 531.90 and 533.61 eV correspond to the crystal lattice O atoms (Bi-O bond), to surface O-H bonds and to C=O bonds present in rGO and in $ZnPc(CO_2H)_4$, respectively (Fig. 6b). The Br peak could be deconvoluted into two signals at 68.53 and 69.58 eV corresponding to Br $3d_{5/2}$ and Br $3d_{3/2}$, respectively (Fig. 6c). For C 1s, the signals observed between 285.01 and 289.41 eV correspond to the various C atoms present in rGO and $ZnPc(CO_2H)_4$ (C-C, C=C, C-O and C=O bonds) and to the adventitious carbon on the surface of the photocatalyst (Fig. 6d). The N 1s spectrum shows two signals at 399.12 and 400.39 eV corresponding to C-N and C=N bonds, respectively [46] (Fig. 6e). Finally, the Zn $2p_{3/2}$ signal at 1021.58 eV confirms that the Zn^{2+} cation is present in the phthalocyanine cavity (Fig. 6f).

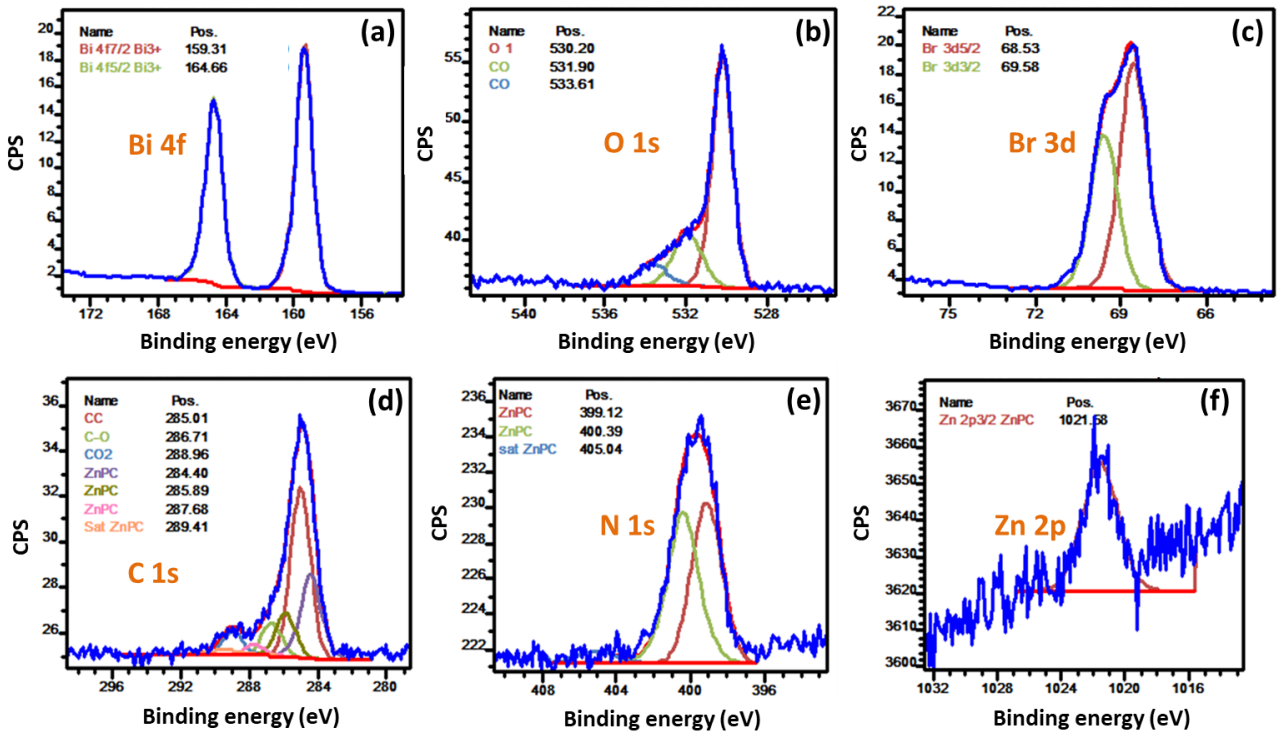

Fig. 6. HR XPS spectra of (a) Bi 4f, (b) O 1s, (c) Br 3d, (d) C 1s, (e) N 1s and (f) Zn 2p.

3.2. Photocatalytic performance of the BiOBr/rGO/ZnPc(CO$_2$H)$_4$ composites

Fig. 7a displays the photocatalytic activity of BiOBr, BiOBr/rGO and of BiOBr/rGO/ZnPc(CO$_2$H)$_4$ samples for the degradation of the Orange II dye under visible light irradiation with an intensity of 13 mW/cm^2. After 30 min of stirring in the dark to reach the adsorption-desorption equilibrium, light was turned on. Under these experimental conditions, the photolysis of Orange II was found to be negligible. The percentage of Orange II adsorbed at the surface of BiOBr/rGO photocatalyst after 30 min in the dark is of ca. 23%. The percentage of the dye absorbed at the surface of the BiOBr/rGO/ZnPc(CO$_2$H)$_4$ catalysts decreased with the loading in ZnPc(CO$_2$H)$_4$ (21, 20 and 15% for loadings in ZnPc(CO$_2$H)$_4$ of 0.1, 0.25 and 0.5 wt%, respectively) likely due to the electrostatic repulsion between Orange II and ZnPc(CO$_2$H)$_4$, both negatively charged at neutral pH.

The photocatalytic activity of pure BiOBr is modest and only 52% of the dye is decomposed after 150 min irradiation. A significant increase of the photodegradation (79%) was observed using the BiOBr/rGO catalyst indicating that rGO improves the lifetime of the photogenerated charge carriers. The photodegradation rate markedly increases when increasing the loading

in $ZnPc(CO_2H)_4$ from 0.1 to 0.25 wt% and almost 98% of Orange II is bleached after 150 min irradiation using the $BiOBr/rGO/ZnPc(CO_2H)_4(0.25)$ catalyst. However, when further increasing the loading in $ZnPc(CO_2H)_4$, the photocatalytic activity shows a downward trend likely due to the high absorption of visible light by $ZnPc(CO_2H)_4$ which weakens the absorption of visible light by the BiOBr/rGO hybrid.

Using the Langmuir-Hinshelwood kinetic model, the apparent pseudo-first-order rate constants k were determined using the formula $\ln(C_0/C_t) = -kt$, where C_0 and C_t are the concentrations of Orange II at t = 0 and at the time t, and were found to be 0.0046, 0.0097, 0.0153, 0.0234 and 0.0191 min^{-1} for BiOBr, BiOBr/rGO, $BiOBr/rGO/ZnPc(CO_2H)_4$ (0.1), $BiOBr/rGO/ZnPc(CO_2H)_4(0.25)$ and $BiOBr/rGO/ZnPc(CO_2H)_4(0.5)$, respectively (Fig. S5).

The primary reactive species involved in the photodegradation of Orange II using the $BiOBr/rGO/ZnPc(CO_2H)_4(0.25)$ catalyst were determined via scavenging experiments using 4-hydroxy-2,2,6,6-tetramethylpiperidine-1-oxyl (TEMPOL), *t*-BuOH, ammonium oxalate (AO), DMSO and NaN_3 to trap superoxide $O_2^{\bullet-}$ radicals, hydroxyl $^{\bullet}OH$ radicals, holes (h^+), electrons (e^-) and singlet oxygen $^1O_2$, respectively (Fig. 7b) [13,27,47]. The inhibition of the photodegradation is the more pronounced using TEMPOL and AO (13 and 19% after 150 min irradiation, respectively), indicating that $O_2^{\bullet-}$ radicals and holes play a key role in the mechanism. All other scavengers only play a minor role (*t*-BuOH and NaN_3) or have no influence (DMSO) on the degradation of the dye.

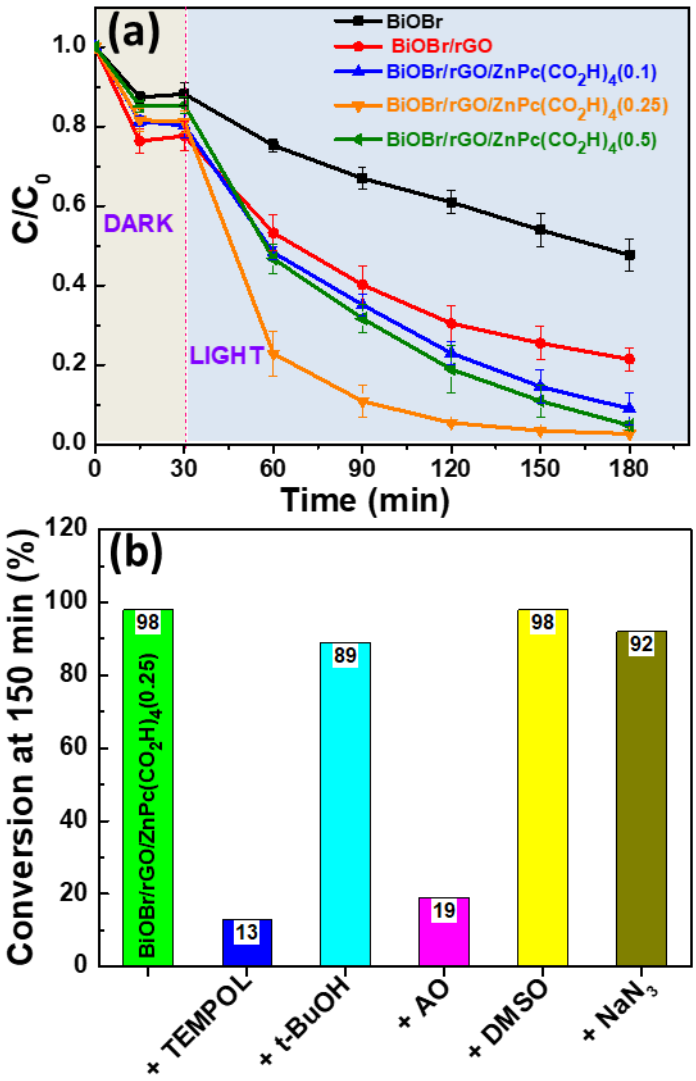

Fig. 7. (a) Photocatalytic activity of BiOBr, BiOBr/rGO, BiOBr/rGO/ZnPc$(CO_2H)_4$(0.25) and BiOBr/rGO/ZnPc$(CO_2H)_4$(0.5) samples for the degradation of Orange II under visible light irradiation. (b) Effects of the TEMPOL, *t*-BuOH, AO, DMSO and NaN_3 scavengers on the photodegradation of Orange II using the BiOBr/rGO/ZnPc$(CO_2H)_4$(0.25) catalyst.

The photodegradation of a more recalcitrant pollutant, in this case phenol, was next investigated. Under visible light irradiation, the degradation kinetics is very slow. Much better results were obtained under simulated solar light irradiation as shown in Fig. 8a and ca. 84% photodegradation can be observed by UV-visible spectroscopy after 180 min irradiation. The self-photodegradation of phenol under simulated solar light irradiation is negligible. The photodegradation of phenol was also monitored by LC-MS and very similar results were

obtained (81% of degradation after 180 min) (Fig. 8b). The rate constant k determined from UV-visible absorption monitoring is of 0.087 min^{-1}.

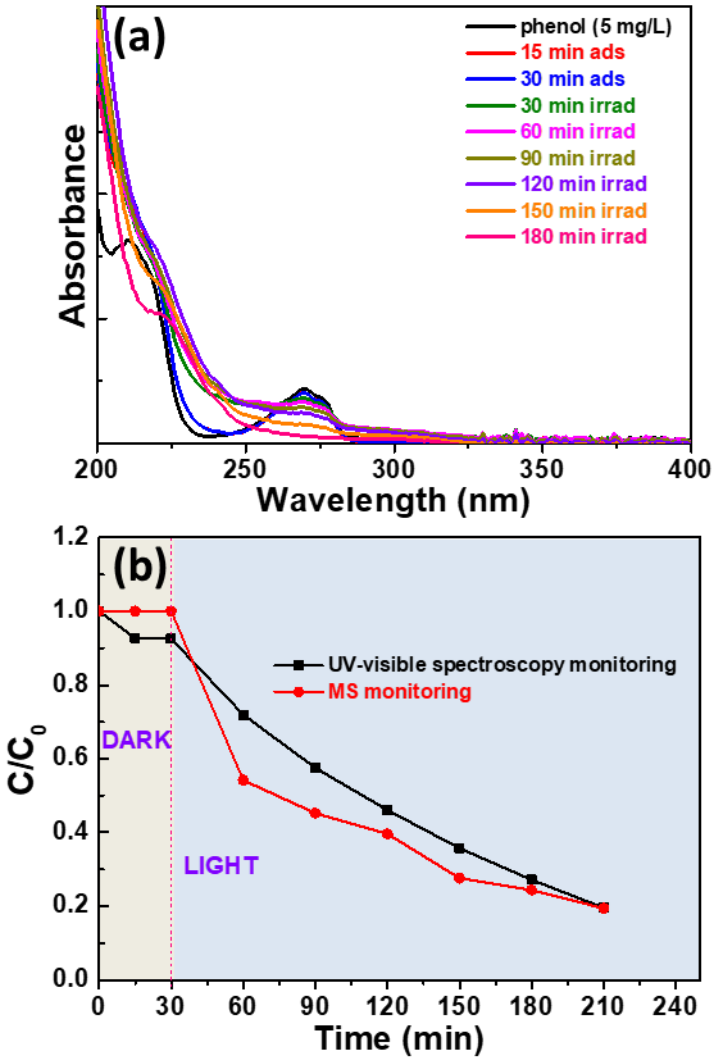

Fig. 8. (a) UV-visible absorption spectra during the photodegradation of phenol using the BiOBr/rGO/ZnPc$(CO_2H)_4$(0.25) catalyst under simulated solar light irradiation. (b) Monitoring of phenol degradation by UV-visible spectroscopy and LC-MS.

Although the experimental conditions (amounts of photocatalyst, light intensity,…) are different from those used in this study, the BiOBr/rGO/ZnPc$(CO_2H)_4$(0.25) catalyst favourably compares with BiOBr-based photocatalysts like BiOBr decorated by C_{70}, ZnO/Nd-doped BiOBr, BiOBr/GO/polyaniline, AgBr/BiOBr/graphene or Pd/BiOBr that were recently developed for the degradation of phenol [48-52].

LC-MS analyses show that hydroquinone, catechol, p- and o-benzoquinone were present at the early stage of the photodegradation. Hydroquinone and catechol (*m/z* = 110) likely originate from the reaction of phenol with $O_2^{\bullet-}$ radicals followed by the reduction of the hydroperoxides obtained after protonation by holes. o- and p-Benzoquinone (*m/z* = 108) may be formed by oxidation of catechol and hydroquinone by the holes present in the VB of the photocatalyst. As previously, hydroxyhydroquinone (*m/z* = 126) is likely formed by reaction of hydroquinone and catechol with $O_2^{\bullet-}$ radicals followed by the reduction of the hydroperoxides. All these compounds are further broken down via opening of the aromatic ring into C4, C3 and C2 dicarboxylic acids like maleic (*m/z* = 116), malonic (*m/z* = 104) and oxalic acid (*m/z* = 90) before decomposition into CO_2 and H_2O. Products detected by LC-MS during the photocatalytic degradation of phenol using the BiOBr/rGO/ZnPc$(CO_2H)_4$(0.25) catalyst are in good agreement with results from the literature using ZnO or BiOI/TiO_2 catalysts [53,54]. The mineralization of phenol was further proved by the decrease of the total organic carbon (TOC) from 3.82 to 1.42 mg/L after 180 min of irradiation.

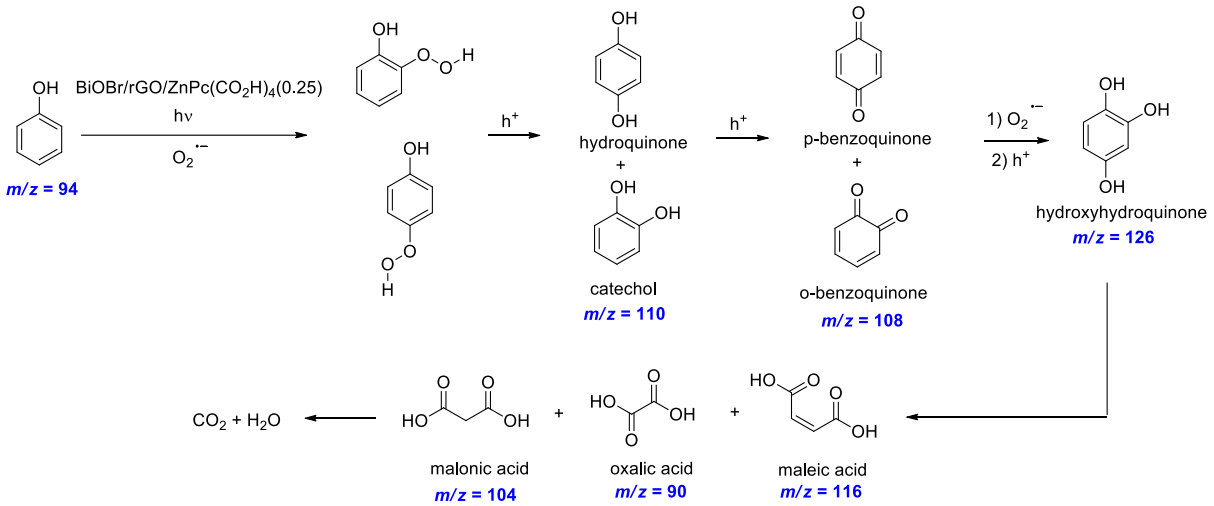

Scheme 2. Mechanism of phenol degradation using the BiOBr/rGO/ZnPc$(CO_2H)_4$(0.25) photocatalyst.

The influence of the photocatalyst loading (15, 30 or 45 mg in 30 mL of solution) on the phenol degradation was investigated (Fig. S6). Similar results were obtained using 30 or 45 mg of the BiOBr/rGO/ZnPc$(CO_2H)_4$(0.25) catalyst (the k values are 0.087 and 0.09 min^{-1}, respectively). The k value decreased to 0.0043 min^{-1} when decreasing the amount of catalyst to 15 mg due to the saturation of the catalytically active sites by phenol.

The Zeta potential of BiOBr, BiOBr/rGO and BiOBr/rGO/ZnPc$(CO_2H)_4$(0.25) catalysts aqueous dispersions as a function of pH was determined. The point of zero charge (pzc) for BiOBr, BiOBr/rGO and BiOBr/rGO/ZnPc$(CO_2H)_4$(0.25) are 3.25, 3.16 and 3.07 (Fig. S7a), which indicates that the surface of the photocatalyst is negatively charged at pH values higher than 3.07. We also varied the pH in the 3-11 range and evaluated its influence on the photodegradation of phenol. As shown in Fig. S7b, the photocatalytic activity is the highest at pH values of 7, 9 and 11 and ca. 80% of phenol is decomposed after 180 min irradiation. A marked decrease of the photodegradation is observed at acidic pH (47 and 26% at pH 5 and 3, respectively).

The stability and the reuse of photocatalysts are key factors regarding practical applications. Fig. 9a shows results obtained for phenol degradation after 180 min using the BiOBr/rGO/ZnPc$(CO_2H)_4$(0.25) catalyst under simulated solar light irradiation (15 mW/cm^2). After each cycle, the photocatalyst was recovered by centrifugation and reused without washing or drying. After ten cycles, only a weak decrease of the photodegradation from 84.4 to 78.4% is observed, indicating the excellent reusability of the photocatalyst. After the ten photodegradation experiments, no crystalline structure changes were observed by XRD which indicates the stability of the photocatalyst (Fig. 9b). Moreover, the amounts of Bi and Zn leached from the photocatalyst were quantified by ICP-OES after a photocatalytic experiment. A very low amount of Bi (ca. 0.08% relative to BiOBr) and no Zn could be detected, further confirming the durability of the BiOBr/rGO/ZnPc$(CO_2H)_4$(0.25) catalyst.

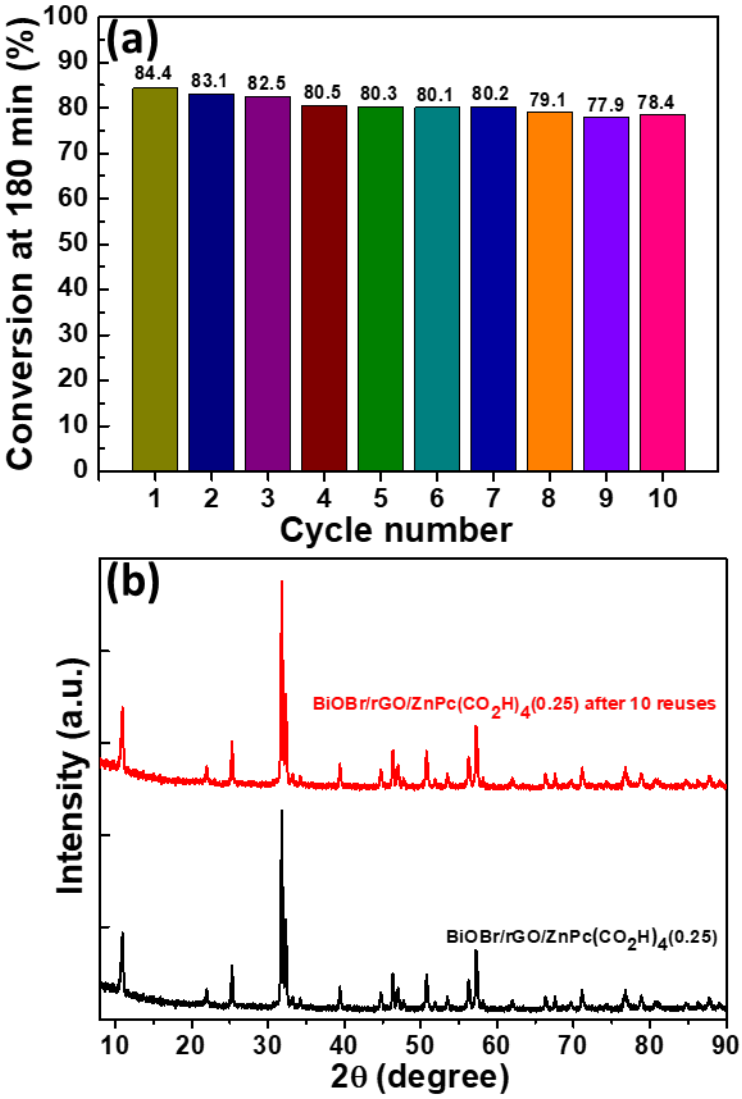

Fig. 9. (a) Phenol photodegradation efficiency after 180 min illumination using the BiOBr/rGO/ZnPc$(CO_2H)_4$(0.25) catalysts for ten cycles. (b) XRD patterns of the BiOBr/rGO/ZnPc$(CO_2H)_4$(0.25) catalyst before and after ten photocatalytic experiments.

3.3. Photocatalytic mechanism

First, photoluminescence (PL) was used to analyze the charge carrier separation efficiency in the photocatalysts. Fig. 10a shows the PL emission spectra of BiOBr, BiOBr/rGO and BiOBr/rGO/ZnPc$(CO_2H)_4$(0.25) samples using an excitation wavelength of 330 nm. BiOBr exhibits a broad PL emission centered at ca. 435 nm. After association with rGO and ZnPc$(CO_2H)_4$, a decrease and a red-shift of the PL emission to 446 nm are observed, indicating that the recombination of photogenerated charge carriers is altered in the composite

photocatalysts likely due to the efficient transfer of photogenerated electrons between BiOBr, rGO and ZnPc$(CO_2H)_4$. It should also be mentioned that the PL emission of ZnPc$(CO_2H)_4$ disappeared indicating that the electron-hole recombination is suppressed in the Pc.

Next, the transient-photocurrent of these samples were recorded for light on-off cycles under visible light irradiation at a potential of 0.5 V (vs Ag/AgCl) in a 0.1 M Na_2SO_4 solution (Fig. 10b). The BiOBr/rGO/ZnPc$(CO_2H)_4$(0.25) catalyst shows a photocurrent density ca. 1.5-fold higher than BiOBr and 3-fold higher than that of BiOBr which indicates an enhanced separation of charge carriers and a fast electron transfer which likely originate from the high interfacial connection between BiOBr, rGO and ZnPc$(CO_2H)_4$.

Finally, electrochemical impedance spectroscopy (EIS) was used to investigate the capacitance and the resistance of the photocatalysts (Fig. 10c). The EIS Nyquist plot of BiOBr/rGO/ZnPc$(CO_2H)_4$ has a much smaller arc radius compared to BiOBr and BiOBr/rGO, indicating a lower charge transfer resistance and thus the efficient separation of photogenerated charge carriers.

The decreased PL intensity combined to the transient photocurrent response and to the EIS Nyquist plot indicate a higher separation efficiency of the photoinduced charge carriers and a lower recombination rate during illumination for the BiOBr/rGO/ZnPc$(CO_2H)_4$(0.25) hybrid catalyst which explain its higher photocatalytic activity.

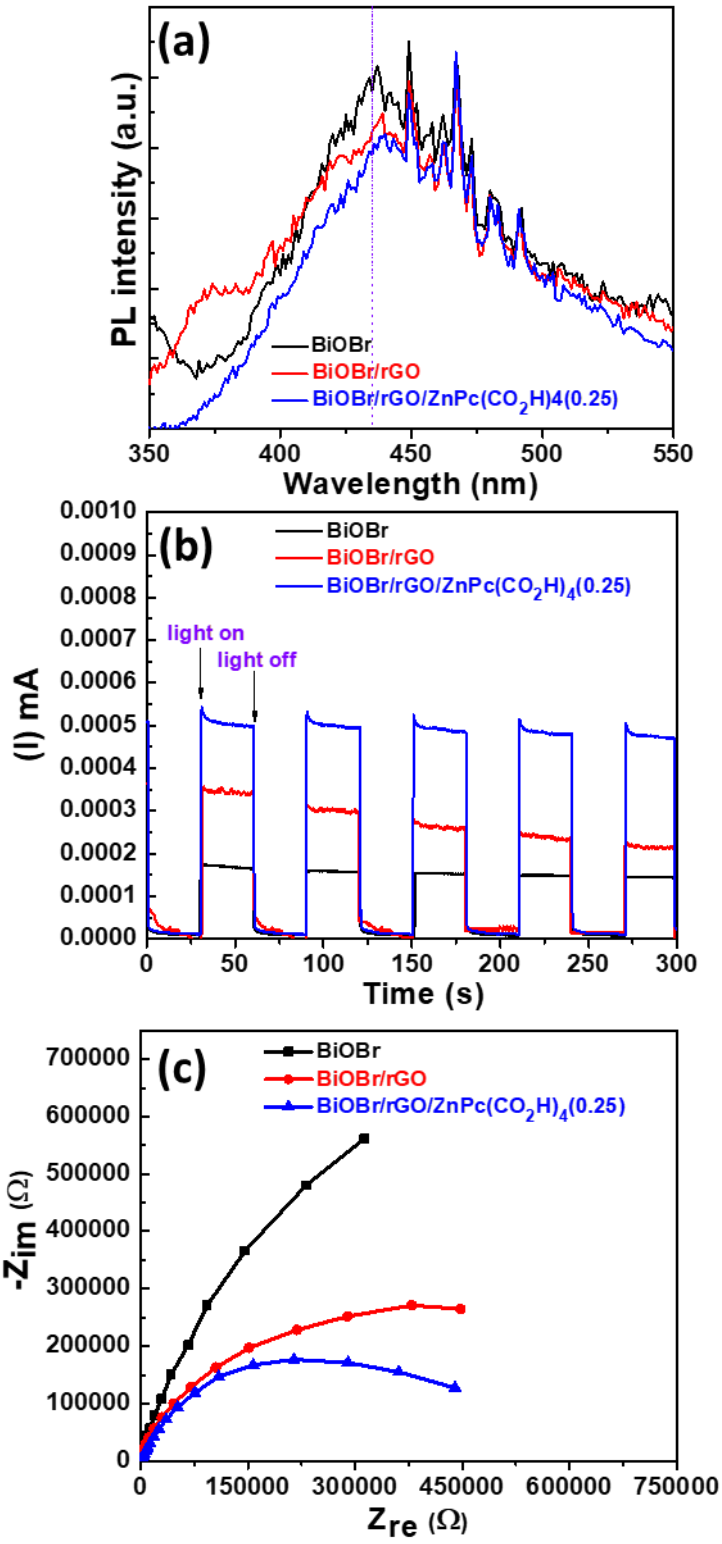

Fig. 10. (a) PL emission spectra (λ_{ex} = 330 nm), (b) transient photocurrent responses, (c) EIS Nyquist plots of BiOBr, BiOBr/rGO, BiOBr/rGO/ZnPc$(CO_2H)_4$(0.25) photocatalysts.

To rationalize the synergistic effect of BiOBr, rGO and $ZnPc(CO_2H)_4$ within the heterostructured catalyst, their electronic structures were determined. The electrochemical potentials of the valence band (VB) and of the conduction band (CB) of BiOBr can be calculated according to the following equations:

$E_{VB} = \chi - E^e + 0.5\ Eg$

$E_{CB} = E_{VB} - Eg$

where χ is the absolute electronegativity of BiOBr (6.176), E^e is the energy of free electrons on the hydrogen scale (ca. 4.5 eV) and Eg is the bandgap (2.85 eV for the BiOBr/rGO/$ZnPc(CO_2H)_4$ (0.25) composite according to DRS results) [55]. The VB and CB edge potentials of BiOBr were estimated to be 3.101 and 0.251 eV vs NHE, respectively.

For $ZnPc(CO_2H)_4$, the estimation of energy levels was conducted through cyclic voltammetry (CV) which allows to measure oxidation potentials and then the HOMO and LUMO values can be calculated [56]. The electrochemical properties of $ZnPc(CO_2H)_4$ were investigated by CV in deoxygenated dimethylformamide (DMF) with tetrabutylammonium hexafluorophosphate ($TBAPF_6$) as the supporting electrolyte in a standard three-electrode cell, composed of a glassy carbon electrode, a platinum counter electrode, and a saturated calomel reference electrode (SCE) LiCl 1M (Fig. 11). In the oxidation part, the cyclic voltammogram reveals especially a first broad redox process, which displays some reversibility. Indeed, differential pulse voltammetry experiment (DPV) exhibits a signal at 0.83 V *vs* SCE attributed to the first oxidation process (Fig. S8). Then the oxidation onset is used to calculate E_{HOMO} and E_{LUMO} using the energy bandgap of $ZnPc(CO_2H)_4$ (Eg = 1.75 eV) (Fig. S9) and the following equations :

$E_{HOMO} = -[(E_{ox}-E_{1/2\ (ferrocene)} + 4.8]$

$E_{LUMO} = E_{HOMO} + E_g$

The HOMO and LUMO levels of $ZnPc(CO_2H)_4$ are of -5.12 eV and -3.27 eV with respect to the vacuum level, respectively, which corresponds to -1.13 and +0.62 eV vs NHE [57].

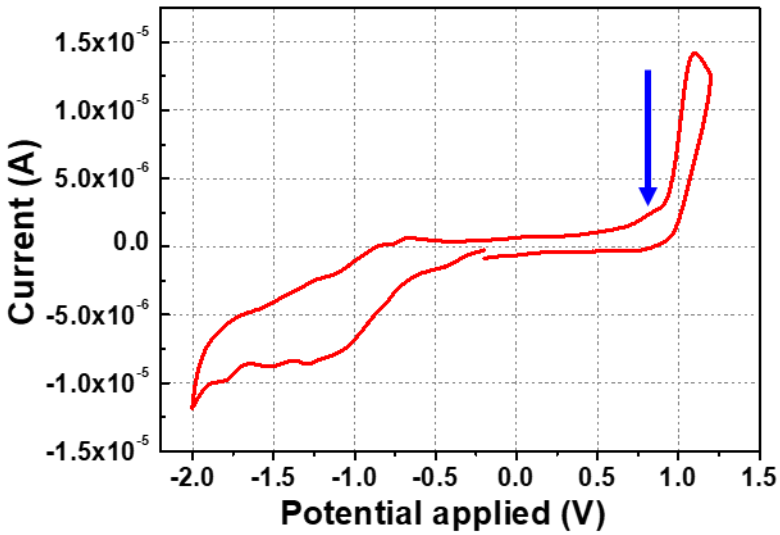

Fig. 11. Cyclic voltammogram of $ZnPc(CO_2H)_4$ in DMF containing 0.1 M $TBAPF_6$.

The mechanism for Orange II and phenol photodegradation can be proposed based on scavenging experiments and on photoelectrochemical measurements. Under visible or simulated solar light irradiation, the electrons in the HOMO of $ZnPc(CO_2H)_4$ and in the VB of BiOBr are excited to the LUMO and CB, respectively, leaving holes in the HOMO and in the VB (Fig. 12a). Since BiOBr is a p-type semiconductor, its Fermi energy level is located near the VB edge. Due to the high working function of rGO (0.08 eV vs NHE) and to the internal electron field at the rGO/BiOBr interface, photogenerated electrons in the CB of BiOBr can easily migrate to rGO [58]. The separation efficiency of photogenerated charge carriers at the interface of BiOBr and rGO is improved by the Schottky barrier [59,60], as previously demonstrated by PL and PEC measurements. As the LUMO of $ZnPc(CO_2H)_4$ is more negative than the CB of BiOBr, photogenerated electrons in $ZnPc(CO_2H)_4$ could also be injected in the CB of BiOBr before being transferred to rGO. However, these electrons can only hardly reduce O_2 into $O_2^{\bullet-}$ radicals since the CB edge potential of BiOBr (0.25 eV vs NHE) and the working function of rGO are more positive than the redox potential of the $O_2/O_2^{\bullet-}$ couple (-0.18 eV vs NHE). These data are inconsistent with the scavenging results which show that $O_2^{\bullet-}$ radicals have a critical role on the photodegradation of Orange II and phenol. Therefore, a Z-scheme mechanism seems more likely for the photodegradation reactions mediated by the $BiOBr/rGO/ZnPc(CO_2H)_4$ catalyst.

The interfacial junction between BiOBr, rGO and $ZnPc(CO_2H)_4$ allows electrons in the CB of BiOBr and delocalized onto rGO to flow to the HOMO of $ZnPc(CO_2H)_4$ and recombine with holes (Fig. 12b). The LUMO of $ZnPc(CO_2H)_4$ (-1.13 eV vs NHE) is more negative than the redox potential of the $O_2/O_2^{\bullet-}$ couple thus allowing photogenerated electrons in the LUMO of $ZnPc(CO_2H)_4$ to reduce O_2 into $O_2^{\bullet-}$ radicals that were demonstrated to oxidize the pollutants into CO_2 and H_2O. The addition of DMSO in the reaction medium has a weak impact on the photodegradation indicating that electrons transferred from BiOBr to rGO and then to $ZnPc(CO_2H)_4$ quickly react with O_2.

The holes in the VB of BiOBr could oxidize H_2O into $^{\bullet}OH$ radicals as the VB of BiOBr (3.10 eV vs NHE) is more positive than the redox potential of the $^{\bullet}OH/H_2O$ couple (2.32 eV vs NHE). However, scavenging experiments show that the direct oxidation of Orange II or phenol seems to be privileged since the addition of the *t*-BuOH scavenger only weakly decreases the degradation. Finally, $^1O_2$ produced either by the reaction of $ZnPc(CO_2H)_4$ in its excited triplet state with $^3O_2$ or by the oxidation of $O_2^{\bullet-}$ by h^+ only weakly contributes to the photodegradation.

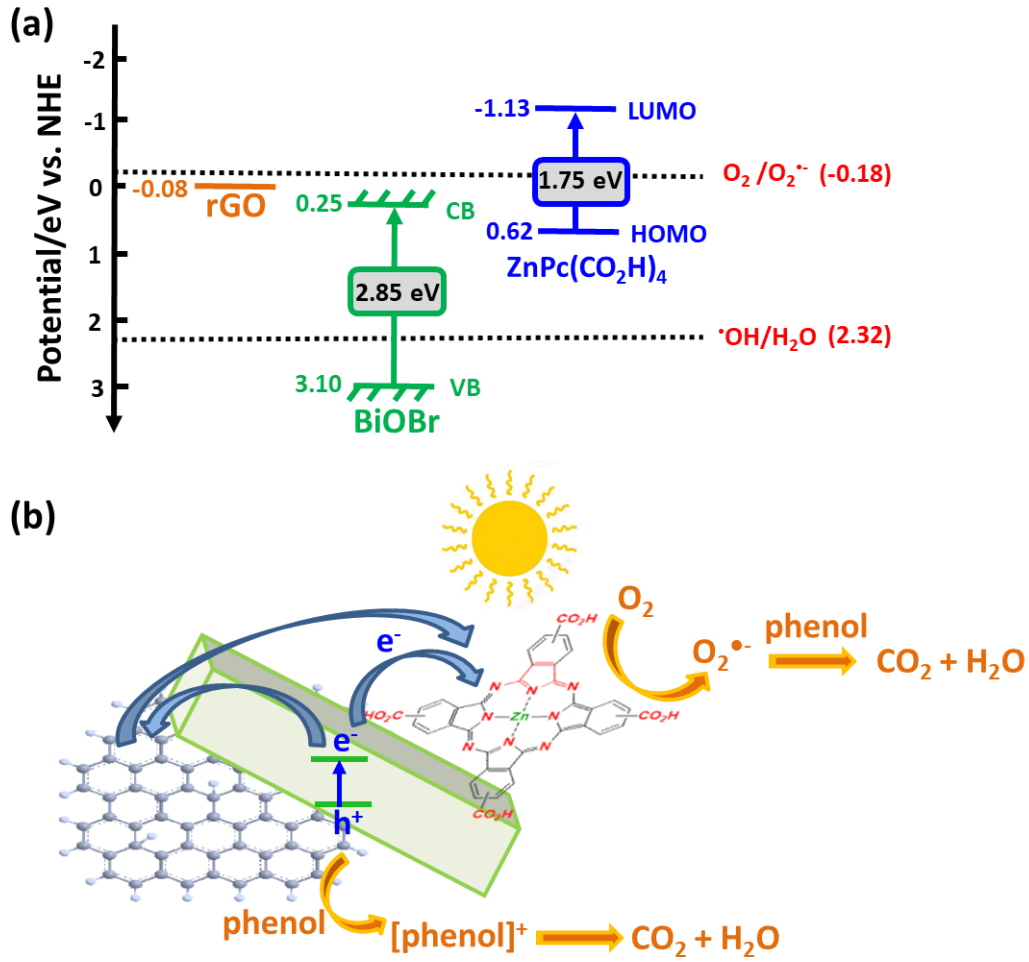

Fig. 12. (a) Energy levels of BiOBr, rGO and $ZnPc(CO_2H)_4$, (b) A proposed Z-scheme mechanism for the photocatalytic degradation of phenol using the BiOBr/rGO/$ZnPc(CO_2H)_4$ catalyst under simulated solar light irradiation.

4. Conclusion

In summary, a three-component photocatalyst associating BiOBr, rGO and $ZnPc(CO_2H)_4$ was synthesized and used for the degradation of Orange II and phenol. Results show that $ZnPc(CO_2H)_4$ is an efficient photosensitizer of BiOBr/rGO and allows to improve its photocatalytic activity, the highest photoactivity being obtained for a loading of 0.25 wt% $ZnPc(CO_2H)_4$ onto BiOBr/rGO. Transient photocurrent responses, EIS Nyquist plots and photoluminescence demonstrate the enhancement of the charge carriers separation efficiency in the BiOBr/rGO/$ZnPc(CO_2H)_4$(0.25) catalyst due to intimate contact between the three components. The active species involved in the photodegradation of Orange II and

phenol are superoxide radicals and holes as showed by scavenging experiments and a Z-scheme mechanism is proposed. The BiOBr/rGO/ZnPc$(CO_2H)_4$(0.25) catalyst can easily be synthesized, exhibits a relatively wide pH tolerance and a high stability. This work highlights the potential of phthalocyanines for the enhancement of the performance of the BiOBr wide bandgap photocatalyst.

CRediT authorship contribution statement

Seydou Ouedraogo: Methodology, Investigation, Data curation, Writing – original draft. **Bilel Chouchene**: Methodology, Investigation, Data curation, Writing – original draft. **Thomas Gries**: Investigation, Data curation, Writing – original draft. **Christophe Desmarets**: Investigation, Data curation, Writing – original draft. **Lavinia Balan**: Investigation, Data curation, Writing – original draft. **Jean-Jacques Gaumet**: Investigation, Data curation. **Ghouti Medjahdi**: Methodology, Investigation, Data curation. **Karifa Bayo**: Supervision, Funding acquisition. **Raphaël Schneider**: Supervision, Conceptualization, Writing – review & editing, Funding acquisition.

Declaration of Competing Interest

The authors declare that they have no known competing financial interests or personal relationships that could have appeared to influence the work reported in this paper.

Acknowledgments

The authors thank Dr Khalid Ferji (LCPM, Université de Lorraine) for Zeta potential measurements.

Appendix A. Supplementary data

Supplementary material related to this article can be found, in the online version, at doi:https://

References

[1] K. Sharma, V. Dutta, S. Sharma, P. Raizada, A. Hosseini-Bandegharaei, P. Thakur, P. Singh, Recent advances in enhanced photocatalytic activity of bismuth oxyhalides for efficient photocatalysis of organic pollutants in water: A review, J. Ind. Eng. Chem. 78 (2019) 1-20.

[2] Y. Yang, C. Zhang, C. Lai, G. Zeng, D. Huang, M. Cheng, J. Wang, F. Chen, C. Zhou, W. Xiong, BiOX (X = Cl, Br, I) photocatalytic nanomaterials: Applications for fuels and environmental management, Adv. Colloid Interface Sci. 254 (2018) 76-93.

[3] X. Wei, M. U. Akbar, A. Raza, G. Li, A review on bismuth oxyhalide based materials for photocatalysis, Nanoscale Adv. 3 (2021) 3353-3372.

[4] Z. Wang, M. Chen, D. Huang, G. Zeng, P. Xu, C. Zhou, C. Lai, H. Wang, M. Cheng, W. Wang, Multiply structural optimized strategies for bismuth oxyhalide photocatalysis and their environmental application, Chem. Eng. J. 374 (2019) 1025-1045.

[5] S. S. Iman, R. Adnan, N. H. M. Kaus, The photocatalytic potential of BiOBr for wastewater treatment: A mini-review, J. Environ. Chem. Eng. 9 (2021) 105404.

[6] D. Zhang, H. Liu, C. Su, H. Li, Y. Geng, Combustion synthesis of highly efficient Bi/BiOBr visible light photocatalyst with synergetic effects of oxygen vacancies and surface plasma resonance, Sep. Purif. Technol. 218 (2019) 1-7.

[7] X. Meng, Z. Li, J. Chen, H. Xie, Z. Zhang, Enhanced visible light-induced photocatalytic activity of surface-modified BiOBr with Pd nanoparticles, Appl. Surf. Sci. 433 (2018) 76-87.

[8] A. C. Mera, H. Valdes, F. J. Jamett, M. F. Melendrez, BiOBr microspheres for photocatalytic degradation of an anionic dye, Solid State Sci. 65 (2017) 15-21.

[9] L. Cao, D. Ma, Z ; Zhou, C. Xu, C. Cao, P. Zhao, Q. Huang, Efficient photocatalytic degradation of herbicide glyphosate in water by magnetically separable and recyclable BiOBr/Fe_3O_4 nanocomposites under visible light irradiation, Chem. Eng. J. 368 (2019) 212-222.

[10] S. Zhang, J. Yang, Microwave-assisted synthesis of BiOCl/BiOBr composites with improved visible-light photocatalytic activity, Ind. Eng. Chem. Res. 54 (2015) 9913-9919.

[11] X. Tu, S. Luo, G. Chen, J. Li, One-pot synthesis, characterization, and enhanced photocatalytic activity of a BiOBr–Graphene composite, Chem. Eur. J. 18 (2012) 14359-14366.

[12] J. Di, J. Xia, M. Ji, B. Wang, S. Yin, Q. Zhang, Z. Chen, H. Li, Advanced photocatalytic performance of graphene-like BN modified BiOBr flower-like materials for the removal of pollutants and mechanism insight, Appl. Catal. B : Environ. 183 (2016) 254-262.

[13] L. Allagui, B. Chouchene, T. Gries, G. Medjahdi, E. Girot, X. Framboisier, A. Ben haj Amara, R. Schneider, Core/shell rGO/BiOBr particles with visible photocatalytic activity towards water pollutants, Appl. Surf. Sci. 490 (2019) 580-591.

[14] S. Fu, W. Yuan, X. Liu, Y. Yan, H. Liu, L. Li, F. Zhao, J. Zhou, A novel 0D/2D WS_2/BiOBr heterostructure with rich oxygen vacancies for enhanced broad-spectrum photocatalytic performance, J. Colloid Interface Sci. 569 (2020) 150-163.

[15] H. Huang, X. Han, X. Li, S. Wang, P. K. Chu, Y. Zhang, Fabrication of multiple heterojunctions with tunable visible-light-active photocatalytic reactivity in BiOBr–BiOI full-range composites based on microstructure modulation and band structures, ACS Appl. Mater. Interfaces 7 (2015) 482-492.

[16] D. Majhi, K. Das, A. Mishra, R. Dhiman, B.G. Mishra, One pot synthesis of CdS/BiOBr/$Bi_2O_2CO_3$: A novel ternary double Z-scheme heterostructure photocatalyst for efficient degradation of atrazine, Appl. Catal. B : Environ. 260 (2020) 118222.

[17] Y. Guo, H. Huang, Y. He, N. Tian, T. Zhang, P.K. Chu, Q. An, Y. Zhang, In situ crystallization for fabrication of a core–satellite structured BiOBr–CdS heterostructure with excellent visible-light-responsive photoreactivity, Nanoscale 7 (2015) 11702-11711.

[18] H. Tang, Y. Deng, H. Zhou, Y. Tan, Y. Xiang, Y. Xu, W. Wu, Y. Zhou, Synthesis of z-scheme $CuInS_2$@BiOBr heterojunction composite with visible-light activity, Chemistry Select 5 (2020) 8258-8264.

[19] L. Kong, Z. Jiang, T. Xiao, L. Lu, M.O. Jones, P. P. Edwards, Exceptional visible-light-driven photocatalytic activity over BiOBr–$ZnFe_2O_4$ heterojunctions, Chem. Commun. 47 (2011) 5512-5514.

[20] F. Cao, J. Wang, Y. Wang, J. Zhou, S. Li, G. Qin, W. Fan, An in situ Bi-decorated BiOBr photocatalyst for synchronously treating multiple antibiotics in water, Nanoscale Adv. 1 (2019) 1124-1129.

[21] W. Guo, Q. Qin, L. Geng, D. Wang, Y. Guo, Y. Yang, Morphology-controlled preparation and plasmon-enhanced photocatalytic activity of Pt–BiOBr heterostructures, J. Hazard. Mater. 308 (2016) 374-385.

[22] Q. Sun, Y. Xu, Sensitization of TiO_2 with aluminum phthalocyanine: factors influencing the efficiency for chlorophenol degradation in water under visible light, J. Phys. Chem. C 113 (2009) 12387-12394.

[23] W. Vallejo, K. Navarro, C. Diaz-Uribe, E. Schott, X. Zarate, E. Romero, Zn(II)-tetracarboxy-phthalocyanine-sensitized TiO_2 thin films as antimicrobial agents under visible irradiation: a combined DFT and experimental study, ACS Omega 6 (2021) 13637-13646.

[24] A. Yarahmadi, S. Sharifnia, Dye photosensitization of ZnO with metallophthalocyanines (Co, Ni and Cu) in photocatalytic conversion of greenhouse gases, Dyes Pigm. 107 (2014) 140-145.

[25] G. M. Neelgund, A. Oki, Z. Luo, ZnO and cobalt phthalocyanine hybridized graphene: Efficient photocatalysts for degradation of rhodamine B, J. Colloid Interface Sci. 430 (2014) 257-264.

[26] W. Lu, T. Xu, Y. Wang, H. Hu, N. Li, X. Jiang, W. Chen, Synergistic photocatalytic properties and mechanism of g-C_3N_4 coupled with zinc phthalocyanine catalyst under visible light irradiation, Appl. Catal. B: Environ. 180 (2016) 20-28.

[27] S. Ouedraogo, B. Chouchene, C. Desmarets, T. Gries, L. Balan, R. Fournet, G. Medjahdi, K. Bayo, R. Schneider, Copper octacarboxyphthalocyanine as sensitizer of graphitic carbon nitride for efficient dye degradation under visible light irradiation, Appl. Catal. A: Gen. 563 (2018) 127-136.

[28] M. Yaghoubi-berijani, B. Bahramian, Synthesis, and new design into enhanced photocatalytic activity of porphyrin immobilization on the surface of bismuth oxyhalides modified with polyaniline, J. Inorg. Organomet. Polym. Mater. 30 (2020) 4637-4654.

[29] M. Yaghoubi-berijani, B. Bahramian, S. Zargari, Synthesis, characterization, and design of a photocatalyst based on BiOBr nanoplates and tin porphyrin with enhanced visible light photocatalytic activity, Res. Chem. Intermed. 46 (2020) 197-213.

[30] X. Guo, X. Zhou, X. Li, C. Shao, C. Han, X. Li, Y. Liu, Bismuth oxychloride (BiOCl)/copper phthalocyanine (CuTNPc) heterostructures immobilized on electrospun polyacrylonitrile nanofibers with enhanced activity for floating photocatalysis, J. Colloid Interface Sci. 525 (2018) 187-195.

[31] L. Zhang, W. Wang, S. Sun, Y. Sun, E. Gao, J. Xu, Water splitting from dye wastewater: A case study of BiOCl/copper(II) phthalocyanine composite photocatalyst, Appl. Catal. B: Environ. 132-133 (2013) 315-320.

[32] S. Yin, Y. Chen, Q. Hu, M. Li, Y. Ding, Y. Shao, J. Di, J. Xia, H. Li, In-situ preparation of iron(II) phthalocyanine modified bismuth oxybromide with enhanced visible-light photocatalytic activity and mechanism insight, Colloids Surf. A Physicochem. Eng. 575 (2019) 336-345.

[33] J. Wang, D. Liu, Q. Liu, T. Peng, R. Li, S. Zhou, Effects of the central metal ions on the photosensitization of metalloporphyrins over carbon nitride for visible-light-responsive H2 production, Appl. Surf. Sci. 464 (2019) 255-261.

[34] P. Zeng, J. Wang, Y. Guo, R. Li, G. Mei, T. Peng, Synthesis of an A_2BC-type asymmetric zinc phthalocyanine derivative for efficient visible/near-infrared-driven H_2 evolution on g-C_3N_4, Chem. Engineer. J. 373 (2019) 651-659.

[35] H. Moussa, E. Girot, K. Mozet, H. Alem, G. Medjahdi, R. Schneider, ZnO rods/reduced graphene oxide composites prepared via a solvothermal reaction for efficient sunlight-driven photocatalysis, Appl. Catal. B: Environ. 185 (2016) 11-21.

[36] J. Nackiewicz, M. Klider, Synthesis and selected properties of metallo and metal-free 2,3,9,10,16,17,23,24–octacarboxyphthalocyanines, Arkivoc i (2015) 269-299.

[37] Y. Liu, M. S. Liu, A. K. Y. Jen, Synthesis and characterization of a novel and highly efficient light-emitting polymer, Acta Polym. 50 (1999) 105-108.

[38] J. H. Tsai, W. Y. Lee, W. C. Chen, C. Y. Yu, G. W. Hwang, C. Ting, New two-dimensional thiophene–acceptor conjugated copolymers for field effect transistor and photovoltaic cell applications, Chem. Mater. 22 (2010) 3290-3299.

[39] C. Lu, H. C. Wu, Y. C. Chiu, W. Y. Lee, W. C. Chen, Biaxially extended quaterthiophene- and octithiophene-vinylene conjugated polymers for high performance field effect transistors and photovoltaic cells, Macromolecules 45 (2012) 3047-3056.

[40] D. Zhang, J. Li, Q. Wang, Q. Wu, High {001} facets dominated BiOBr lamellas: facile hydrolysis preparation and selective visible-light photocatalytic activity, J. Mater. Chem. A 1 (2013) 8622-8629.

[41] D. R. Tackley, G. Dent, W. E. Smith, Phthalocyanines: structure and vibrations, Phys. Chem. Chem. Phys. 3 (2001) 1419-1426.

[42] B. J. Palys, G. J. Puppels, D. van den Ham, D. Feil, Raman spectra of zinc phthalocyanine monolayers adsorbed on glassy carbon and gold electrodes by application of a confocal Raman microspectrometer, J. Electroanal. Chem. 326 (1992) 105-112.

[43] Z. Chen, J. Zeng, J. Di, D. Zhao, M. Ji, J. Xia, H. Li, Facile microwave-assisted ionic liquid synthesis of sphere-like BiOBr hollow and porous nanostructures with enhanced photocatalytic performance, Green Energy Environ. 2 (2017) 124-133.

[44] E. Marais, R. Klein, E. Antunes, T. Nyokong, Photocatalysis of 4-nitrophenol using zinc phthalocyanine complexes, J. Mol. Catal. A: Chem. 261 (2007) 36-42.

[45] J. Xia, S. Yin, H. Li, H. Xu, L. Xu, Y. Xu, Improved visible light photocatalytic activity of sphere-like BiOBr hollow and porous structures synthesized via a reactable ionic liquid, Dalton Trans. 40 (2011) 5249-5257.

[46] J. Zhu, Y. Li, Y. Chen, J. Wang, B. Zhang, J. Zhang, W.J. Blau, Graphene oxide covalently functionalized with zinc phthalocyanine for broadband optical limiting, Carbon 49 (2011) 1900-1905.

[47] S. Li, X. Shen, J. Liu, L. Zhang, Synthesis of Ta_3N_5/Bi_2MoO_6 core-shell fiber-shaped heterojunctions as efficient and easily recyclable photocatalysts, Environ. Sci. Nano 4 (2017) 1155-1167.

[48] D. Ma, X. Tang, X. Liu, M. Zhao, R. Peng, J. Li, J. Zhong, R. Duan, Enhanced photocatalytic degradation of phenol and rhodamine B over flower-like BiOBr decorated C_{70}, Mater. Res. Bull. 118 (2019) 110521.

[49] J.-C. Sin, C.-A. Lim, S.-M. Lam, A.R. Mohamed, H. Zeng, Facile synthesis of novel ZnO/Nd-doped BiOBr with boosted visible light photocatalytic degradation of phenol, Mater. Lett. 248 (2019) 20-23.

[50] X. Liu, L. Cai, A novel double Z-scheme BiOBr-GO-polyaniline photocatalyst: Study on the excellent photocatalytic performance and photocatalytic mechanism, Appl. Surf. Sci. 483 (2019) 875-887.

[51] P. Singh, Sonu, P. Raizada, A. Sudhaik, P. Shandilya, P. Thakur, S. Agarwal, V.K. Gupta, Enhanced photocatalytic activity and stability of AgBr/BiOBr/graphene heterojunction for phenol degradation under visible light, J. Saudi Chem. Soc. 23 (2019) 586-599.

[52] X. Meng, Z. Li, Z. Zhang, Highly efficient degradation of phenol over a Pd-BiOBr Mott-Schottky plasmonic photocatalyst, Mater. Res. Bull. 99 (2018) 471-478.

[53] C. Feng, Z. Chen, J. Jing, J. Hou, The photocatalytic phenol degradation mechanism of Ag-modified ZnO nanorods, J. Mater. Chem. C 8 (2020) 3000-3009.

[54] B. Li, X. Chen, T. Zhang, S. Jiang, G. Zhang, W. Wu, X. Ma, Photocatalytic selective hydroxylation of phenol to dihydroxybenzene by $BiOI/TiO_2$ p-n heterojunction photocatalysts for enhanced photocatalytic activity, Appl. Surf. Sci. 439 (2018) 1047-1056.

[55] Y. Xu, M. A. A. Schoonen, The absolute energy positions of conduction and valence bands of selected semiconducting minerals, Am. Mineral. 85 (2000) 543-556.

[56] M. Al-Ibrahim, H.-K. Roth, M. Schroedner, A. Konkin, U. Zhokhavets, G. Gobsch, P. Scharff, S. Senfuss, The influence of the optoelectronic properties of poly(3-alkylthiophenes) on the device parameters in flexible polymer solar cells, Organic Electronics 6 (2005) 65-77.
[57] M. D. Archer and A. J. Nozik, Eds., Nanostructured and Photoelectrochemical Systems for Solar Photon Conversion, Imperial College Press, 2008.
[58] M. Zhu, Y. Dong, B. Xiao, Y. Du, P. Yang, X. Wang, Enhanced photocatalytic hydrogen evolution performance based on Ru-trisdicarboxybipyridine-reduced graphene oxide hybrid, J. Mater. Chem. 22 (2012) 23773-23779.
[59] Y. S. Chen, J. C. Crittenden, S. Hackney, L. Sutter, D. W. Hand, Preparation of a novel TiO_2-based p-n junction nanotube photocatalyst, Environ. Sci. technol. 39 (2005) 1201-1208.
[60] Z. Ai, W. Ho, S. Lee, Efficient visible light photocatalytic removal of NO with BiOBr-graphene nanocomposites, J. Phys. Chem. C 115 (2011) 25330-25337.